A&A 465, 71–85 (2007)
DOI: 10.1051/0004-6361:20066187

Astronomy & Astrophysics

Kinematics of the Local Universe

XIII. 21-cm line measurements of 452 galaxies with the Nançay radiotelescope, *JHK* Tully-Fisher relation, and preliminary maps of the peculiar velocity field⋆

G. Theureau[1,2], M. O. Hanski[1,3], N. Coudreau[2], N. Hallet[2], and J.-M. Martin[2]

[1] LPCE/CNRS UMR6115, 3A Av. de la recherche scientifique, 45071 Orléans Cedex 02, France
e-mail: theureau@cnrs-orleans.fr
[2] Observatoire de Paris/Meudon, GEPI/CNRS URA1757, 92195 Meudon Principal Cedex, France
[3] Tuorla observatory, University of Turku, 21500 Piikkiö, Finland

Received 4 August 2006 / Accepted 3 November 2006

ABSTRACT

Aims. This paper presents 452 new 21-cm neutral hydrogen line measurements carried out with the FORT receiver of the meridian transit Nançay radiotelescope (NRT) in the period April 2003–March 2005.
Methods. This observational programme is part of a larger project aiming at an exhaustive and magnitude-complete HI extragalactic catalogue for Tully-Fisher applications (the so-called KLUN project, for Kinematics of the Local Universe studies, to end in 2008). The whole on-line HI archive of the NRT today contains reduced HI-profiles for 4500 spiral galaxies of declination $\delta > -40°$ (http://klun.obs-nancay.fr).
Results. As an example of this application, we used the direct Tully-Fisher relation in three (*JHK*) bands in deriving distances to a large catalogue of 3126 spiral galaxies distributed through the whole sky and sampling the radial velocity range well between 0 and 8000 km s^{-1}. Thanks to an iterative method accounting for selection bias and smoothing effects, we show a detailed and original map of the velocity field in the Local Universe as a preliminary output.

Key words. astronomical data bases: miscellaneous – surveys – galaxies: kinematics and dynamics – radio lines: galaxies

1. Introduction

The present paper complements the KLUN[1] data-series (I: Bottinelli et al. 1992; II: Bottinelli et al. 1993; III: di Nella et al. 1996; VII: Theureau et al. 1998a; XII: Paturel et al. 2003b; Theureau et al. 2005) with a collection of HI line measurements acquired with the Nançay radiotelescope (FORT). This programme has been labelled as a key project of the instrument and allocated on average 20% of the observing time since the first light in mid 2000.

The input catalogue was compiled from the Hyperleda extragalactic database, the 2.7 million galaxy catalogue extracted from the DSS (Paturel et al. 2000), and the releases of DENIS (DEep Near Infrared Survey, Mamon et al. 2004) and 2MASS (2 Micron All Sky Survey, Jarret et al. 2000) near infrared CCD surveys. The aim of the programme is to build a large all-sky sample of spiral galaxies, that is complete down to well-defined magnitude limits in the five photometric bands B, I, J, H, and K, and to allow a peculiar velocity mapping of galaxies up to 10 000 km s^{-1} in radial velocity, i.e. up to a scale greater than the largest structures of the Local Universe.

This programme complements other large HI projects such as HIPASS[2] in Parkes (Barnes et al. 2001) or the ALFA-project at Arecibo[3]. The majority of the objects we observed from Nançay are in the range $-40°$, $+0°$ in declination, thus favouring the declination range unreachable by Arecibo. Our aim was to fill the gaps left in the last Hyperleda HI compilation by Paturel et al. (2003b) in order to obtain well-defined selection criteria in terms of redshift coverage and magnitude completeness (see Sect. 3).

This kind of HI data is crucial for constraining the gas and total mass function of spiral galaxies as a function of morphology and environment. It also allows the mapping of the total mass distribution from peculiar velocities and thus provides strong constraints on cosmological models and large-scale structure formation. They can in particular provide a unique starting point for total mass power spectrum studies.

Study of peculiar velocities allows the current theory of cosmological structure formation by gravitational instability to be verified. It gives information on bulk motions, and the value of Ω_m (cf. reviews by Willick 2000; Zaroubi 2002; and the comprehensive work by Strauss & Willick 1995). The peculiar velocity measurements were obtained using redshift-independent secondary distance indicators, such as the Tully-Fisher (TF) relation for spiral galaxies, the Faber-Jackson, D_n-σ, Fundamental Plane (FP) relation, or the surface brightness fluctuations for early type galaxies. The largest surveys so far are the Mathewson & Ford (1996) sample, the MARK III (Willick et al. 1997), SFI (Giovanelli et al. 1997; Haynes et al. 1999), ENEAR (da Costa et al. 2000a,b), and the updated FGC catalogue (2MFGC, Mitronova et al. 2004). Each contains about one or two thousand

⋆ Data Tables 2, 3, and 5 and HI-profiles (Fig. 4) are only available in electronic form at the CDS via anonymous ftp to cdsarc.u-strasbg.fr (130.79.128.5) or via http://cdsweb.u-strasbg.fr/cgi-bin/qcat?J/465/71

[1] for Kinematics in the Local UNiverse.

[2] http://www.atnf.csiro.au/research/multibeam/release/

[3] http://alfa.naic.edu/alfa/

independent distance estimates in the local 80 h^{-1} Mpc volume. We then compared them to the velocity field derived from the galaxy density distribution as inferred from a complete redshift sample (e.g. PSCz, Saunders et al. 2000; or NOG, Marinoni et al. 1998)

Our own Kinematics of the Local UNiverse (KLUN) TF sample was used in the study of H_0 (Theureau et al. 1997; Ekholm et al. 1999) and local structures (Hanski et al. 2001). The sample consists of all the galaxies with published rotational velocities collected in the Hyperleda[4] database (Paturel et al. 2003a), plus the recent large KLUN+ contribution (Theureau et al. 2005; and this paper). The total Tully-Fisher sample counts 15 700 spirals and uses five different wavelength galaxy magnitudes. The B- and I-magnitudes come from various sources, carefully homogenized to a common system. The largest sources are DSS1 for B, and Mathewson et al. (1992, 1996) and DENIS (Paturel et al. 2004) for I band. The J, H, and K-magnitudes are from the 2MASS[5] survey (Jarret et al. 2000). The 2MASS magnitudes, taken from a single survey, avoid any problems that the homogenization may cause, and are thus exclusively used in data analysis. Furthermore, we exclude the measurements with large errors and those galaxies that for other reasons, explained later in the text, are unsuitable for this study. Of these, 3126 galaxies remain, which we use for mapping the peculiar velocity field within the radius of 80 h^{-1} Mpc.

The paper is structured as follows. The Nançay radiotelescope, the processing chain, and the reduced HI data are presented in Sect. 2. The characteristics of the input Tully-Fisher catalogue are listed in Sect. 3, while the iterative method of obtaining unbiased peculiar velocities from it is given in Sect. 4. Finally, we give some preliminary results in Sect. 5 and show some examples of peculiar velocity-map realization.

2. The HI data

2.1. The Nançay observations

The Nançay radiotelescope (France) is a single-dish antenna with a collecting area of 6912 m^2 (200 × 34.56) equivalent to that of a 94 m-diameter parabolic dish. The half-power beam width at 21-cm is 3.6 arcmin (EW) × 22 arcmin (NS) (at zero declination). The minimal system temperature at $\delta = 15°$ is about 35 K in both horizontal and vertical polarizations. The spectrometer is a 8192-channel autocorrelator offering a maximal bandwidth of 50 MHz. In this mode and with two banks in vertical and horizontal polarizations counting 4096 channels each, the spacing of the channels corresponds to 2.6 km s^{-1} at 21 cm. After boxcar smoothing, the final resolution is typically ∼10 km s^{-1}. The 50 MHz bandwidth is centred on ∼1387 MHz, thus corresponding to an interval of 10 500 km s^{-1} centred on a velocity of 7000 km s^{-1} (except for the few objects with a radial velocity known to be less than 2000 km s^{-1}, for which the observing band was centred on 5000 km s^{-1}). The relative gain of the antenna was calibrated according to Fouqué et al. (1990); the final HI-fluxes (Table 2) were calibrated using a set of well-defined radio continuum sources observed each month as templates.

One "observation" is a series of ON/OFF observational sequences; each sequence is made of ten elementary integrations of 4 s each, plus a set of 3 integrations of 2 s for the calibration, in each cycle adding up to 40 + 6 s for the source and 40 + 6 s for the comparison field. The comparison field is taken at exactly the same positions of the focal track as the source in the same cycle. In this way one minimises the difference between ON and OFF total power efficiently. A typical meridian transit observation lasts about 35 min and is centred on the meridian, where the gain is known to be at its maximum; it contains a series of ∼20 ON/OFF cycles.

The processing chain consists of selecting good elementary integrations or cycles, masking and interpolating areas in the time-frequency plane, straightening the base-line by a polynomial fit (order in the range 1–6), and applying a boxcar smoothing. The maximum of the line profile is determined by eye as the mean value of the maxima of its two horns after taking the rms noise into account (estimated in the base-line). The widths, measured at the standard levels of 20% and 50% of that maximum, correspond to the "distance" separating the two external points of the profile at these intensity levels. The signal-to-noise ratio is the maximum of the line (see above) over rms noise in the baseline-fitted region.

The total list of corrected HI-astrophysical parameters (Table 2), 21-cm line profiles (Fig. 3) and comments concerning the profiles (Table 3), are available in electronic form at the CDS.

2.2. Sample characteristics and data description

In the first five years of observations (2001–2005) since the upgrade of the Nançay receiver (FORT), we have observed 2500 galaxies, successfully detected about 1600 of them, and fully reduced 1340 HI profiles.

As a second KLUN+ release, we present here the spectra obtained for 452 of these galaxies, observed between April 2003 and March 2005. Some simple statistics are presented in Fig. 2. The upper panel shows a comparison of some of our HI-line width at the 20% level with equivalent measurements (W_{P20}) found in the last large compilation of line widths by Springob et al. (2005). The overlap is quite small, concerning only 20 galaxies. The few outlying galaxies are identified either as a distorted HI-line, at the limit of detectability or HI-confused with another neighbouring galaxy (cases of pgc2350, pgc20363, pgc67934, pgc66850, and pgc54825, see Table 3). The other ones are well-aligned on the first bisecting line. One could guess a small systematic effect there: a slight over-estimation of the line width for large widths with respect to the H_α or Arecibo measurement. This is explained easily by the general low signal-to-noise ratio we have for edge-on galaxies, in the range of fluxes we are concerned with. The middle panel shows the distribution of signal-to-noise ratio as a function of 20% level line width W_{20}, and the bottom panel shows the rms noise σ in mJy (outside the 21-cm line) versus integration time.

Table 2 contains all the reduced HI parameters and Table 3 provides corresponding comments, when necessary, for each galaxy. Comments concern mainly object designation, peculiar morphologies or peculiar HI line shape, spectrum quality, and HI confusions. The spectra and extracted data are assigned a quality code. A flag "?" or "*" warns of suspected or confirmed HI line confusion. The five quality classes are defined as follows:

- A: high-quality spectrum, high signal-to-noise and well-defined HI profile;
- B: good signal-to-noise ratio, line border well defined, still suitable for Tully-Fisher applications;
- C: low signal-to-noise, noisy or asymmetrical profile. Well detected, but one should not trust the line width. The radial velocity is perfectly determined;

[4] http://leda.univ-lyon1.fr
[5] http://www.ipac.caltech.edu/2mass/

Table 1. Statistics of the detected galaxies vs. HI profile class.

Profile class	Nb of galaxies
A	84
B	179
C∗	161
D	28
E	101

∗ Among the "C" galaxies, 38 were flagged as HI confused.

- D: low signal-to-noise and noisy profile at the limit of detection. Probably detected, but even the radial velocity could be doubtful;
- E: not detected. The absence of detection, corresponding to the "E" code in the notes, is due to several possible causes: either the object was too faint in HI to be detected within a reasonable integration time (120 full ON/OFF cycles, equivalent to 3 meridian transits), which is probably the predominant case, or else we did not know its radial velocity and it fell outside the frequency range, or the HI line was always behind a radar emission or an interference. In a few cases, some standing waves are clearly visible in the full bandwidth plots (50 MHz ≡ 10 500 km s^{-1}). These are due to reflexions either in the cables, or between the primary and secondary mirrors, or between the secondary and tertiary mirrors. This happens when a strong radiosource (often the Sun) is close to the main beam of the antenna. Finally, when "no detection" is stated, the line was expected to fall within the observed frequency band and the value of the noise gives a fair upper limit for the HI signal.

The distribution of the targets among the different classes is summarised in Table 1. The Aitoff projection of the catalogue in J2000 equatorial is seen in Fig. 1, together with the distribution of the radial velocities and HI fluxes. Most of the observed objects are in the range 4000–10 000 km s^{-1} where the lack of Tully-Fisher measurements in the literature is the most critical.

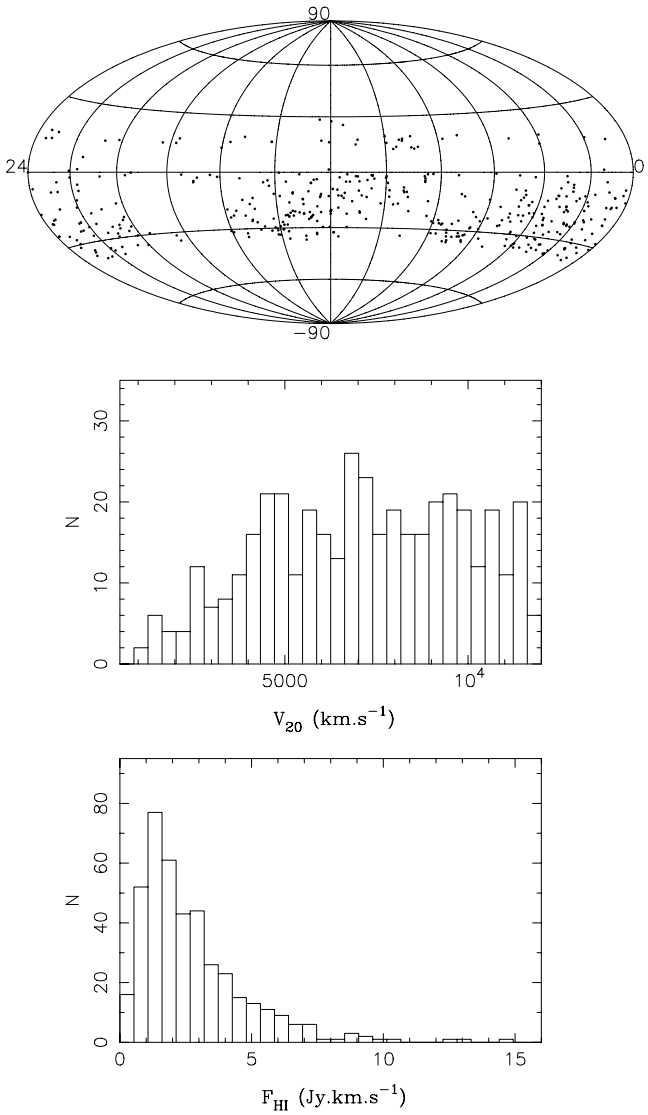

Fig. 1. Aitoff projection of the observed sample in J2000 equatorial coordinates, histogram of radial velocities V_{20} and HI fluxes (see Table 2).

2.3. Data description

Radial velocities Our observed radial velocities are listed in Table 2 (Col. 4) and correspond to the median point of the 21-cm line profile measured at 20% of maximum intensity. The internal mean error on V_{20} is calculated according to Fouqué et al. (1990) as:

$$\sigma(V_{20}) = \frac{4 \cdot (R \cdot \alpha)^{1/2}}{S/N},$$

where R is the actual spectral resolution, $\alpha = (W_{20} - W_{50})/2$ is the slope of the line profile, and S/N is the signal-to-noise ratio. The average of $\sigma(V_{20})$ is about 8 km s^{-1}.

Line widths. Line widths are measured on the observed profile at two standard levels corresponding to 20% and 50% of the maximum intensity of the line. The results listed in Table 2, Cols. 6 and 9, have been corrected to the optical velocity scale. We also provide line widths corrected for resolution effect (Fouqué et al. 1990) in Cols. 7 and 10. The mean measurement error is taken equal to $3 \cdot \sigma(V_{20})$ and $2 \cdot \sigma(V_{20})$ for the 20% and 50% widths, respectively. The data presented here are not corrected for internal velocity dispersion. Details about these corrections can be found in Bottinelli et al. (1990), Fouqué et al. (1990), or in Paturel et al. (2003b).

HI-fluxes. The detailed description of the flux calibration is given in Theureau et al. (2005). HI-fluxes F_{HI} (Table 2, Col. 12) are expressed in Jy km s^{-1}. The values given in Col. 13 are corrected for beam-filling according to Paturel et al. (2003b):

$$F_{HIc} = B_f \cdot F_{HI}$$

where F_{HI} is the observed raw HI-flux,

$$B_f = \sqrt{(1 + xT)(1 + xt)}$$

$$T = (a_{25}^2 \sin^2\beta + b_{25}^2 \cos^2\beta)/\theta_{EW}^2$$

$$t = (a_{25}^2 \cos^2\beta + b_{25}^2 \sin^2\beta)/\theta_{NS}^2$$

where θ_{EW} and θ_{NS} are the half-power beam dimensions of the Nançay antenna, β the position angle of the galaxy defined northeastwards, and a_{25} and b_{25} are the photometric major and minor axis, respectively. The parameter x is $x = 0.72 \pm 0.06$ (Bottinelli et al. 1990). The distribution of the East-West projection of D_{25} diameters is shown in Fig. 2. This is to be compared to the 4 arcmin width of the half-power beam.

Table 2. Astrophysical HI-parameters. Available only in electronic form at the CDS.
Column 1: PGC or LEDA galaxy name;
Col. 2: most usual galaxy name;
Col. 3: J2000 equatorial coordinates;
Col. 4: systemic heliocentric radial velocity (km s^{-1});
Col. 5: rms error (km s^{-1});
Col. 6: total line width at 20% of the maximum intensity (km s^{-1});
Col. 7: total corrected line width at 20% (km s^{-1});
Col. 8: rms error (km s^{-1});
Col. 9: total line width at 50% of the maximum intensity (km s^{-1});
Col. 10: total corrected line width at 50% (km s^{-1});
Col. 11: rms error (km s^{-1});
Col. 12: observed HI-flux (Jy km s^{-1});
Col. 13: beam-filling corrected HI-flux (Jy km s^{-1});
Col. 14: rms error (Jy km s^{-1});
Col. 15: signal-to-noise ratio;
Col. 16: rms noise;
Col. 17: quality code (see Sect. 2);
Col. 18: flag ("c" indicates confirmed HI confusion with the emission of another galaxy; "?" means that confusion is suspected but not certain).

Table 3. Notes on HI-observations. Available only in electronic form at the CDS.
Column 1: PGC or LEDA galaxy name;
Col. 2: morphological type from Hyperleda;
Col. 3: logarithm of isophotal D_{25} diameter in 0.1 arcmin from Hyperleda;
Col. 4: Major axis position angle (North Eastwards) from Hyperleda;
Col. 5: quality code and HI-confusion flag "c" (confirmed) or "?" (possible) (see Sect. 3);
Col. 6: comments; conf = "HI confusion", comp = "companion", cf = "comparison field", poss = "possible", w = "with".

3. Building the Tully-Fisher sample

3.1. The input data

Rotational velocities Rotational velocities, i.e. the $\log V_{\rm m}$ parameter used in the Tully-Fisher relation, were mainly gathered from the Hyperleda compilation (16 666 galaxies, Paturel et al. 2003a) and were complemented by some of our own recent HI line measurements with the Nançay radiotelescope (586 late type galaxies, Theureau et al. 2005). A few other measurements from Haynes et al. (1999) not previously in Hyperleda were also added. All our own 3300 HI spectra acquired with the Nançay radiotelescope antenna in the past decade were reviewed and assigned a quality code according to the shape of their 21-cm line profile. This study (Guilliard et al. 2004) allowed us to efficiently flag several TF outliers due to morphological-type mismatch or HI-confusion in the elongated beam of Nançay. Even if this Nançay subsample concerns only a part of the data (∼25%), we substantially improved the apparent scatter of the TF relation.

In the Hyperleda compilation, the $\log V_{\rm m}$ parameter is calculated from 21-cm line widths at different levels and/or rotation curves (generally in H_α). The last compilation provides us with 50 520 measurements of 21-cm line widths or maximum rotation velocity. These data are characterised by some secondary parameters: telescope, velocity resolution, level of the 21-cm line width. For data homogenisation, HYPERELEDA uses the so-called EPIDEMIC METHOD (Paturel et al. 2003b). One starts from a standard sample (a set of measurements giving a large and homogeneous sample: here, the Mathewson et al. 1996 data), all other measurements are grouped into homogeneous classes (for instance, the class of measurements made at a given level and obtained with a given resolution). The most populated class is cross-identified with the standard sample in order to establish the equation of conversion to the standard system. Then, the whole class is incorporated into the standard sample, so the standard sample grows progressively. The conversion to the standard propagates like an epidemic. In summary, this kind of analysis consists in directly converting the widths for a given resolution r and given level l into a quantity that is homogeneous to twice the maximum rotation velocity (=log W, uncorrected for inclination. A final correction is applied reference by reference to improve the homogenisation.

The final $\log V_{\rm m}$ value is corrected for inclination: $\log V_{\rm m} = (\log W - \log(2 \sin incl))$. Where the inclination $incl$ is derived following RC3 (de Vaucouleurs 1991):

$$\sin^2(incl) = \frac{1 - 10^{2 \log R_{25}}}{1 - 10^{2 \log r_0}}$$

where R_{25} is the axis ratio in B at the isophot corresponding to 25 mag arcsec^{-2}, $\log r_0 = 0.43 + 0.053T$ for type $T = 1$ to 7 (Sa–Sd), and $\log r_0 = 0.38$ for $T = 8$ (Sdm).

Magnitudes. The 2MASS survey, carried out in the three infrared bands J, H, and K, collected photometric data for 1.65 million galaxies with $K_{\rm s} < 14$ (Jarrett et al. 2000) and made the final extended source catalogue public recently. Total magnitude uncertainties for the 2MASS extended objects are generally better than 0.15 mag. We excluded any galaxy with the accuracy of magnitudes worse than 0.3. This accuracy appears reasonable when considering that it is almost impossible to obtain total magnitudes better than 0.1, due to the difficulty of extrapolating the profile reliably.

Extinction. The extinction correction we applied includes a Galactic component, $a_{\rm G}$, adopted from Schlegel et al. (1998), and a part due to the internal absorption of the observed galaxy, $a_{\rm i}$. Both depend on the wavelength.

$$a_{\rm ext} = f_{\rm G}(\lambda) a_{\rm G} + f_{\rm i}(\lambda) a_{\rm i}, \quad (1)$$

where the Galactic and internal wavelength conversion factors are $f_{\rm G}(\lambda) = 1.0, 0.45, 0.21, 0.13, 0.085$ (Schlegel et al. 1998),

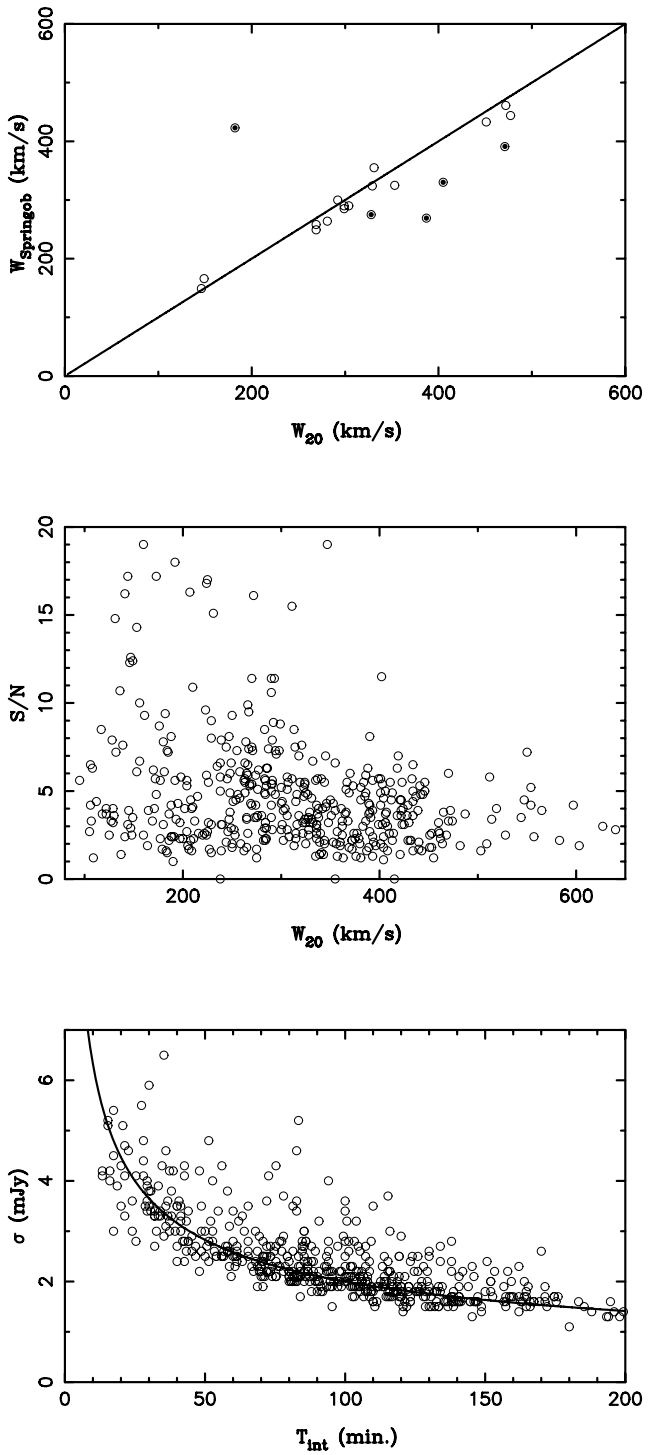

Fig. 2. *Top*: comparison of some of our HI-line width at the 20% level with some independent measurements from Springob et al. (2005). *Middle*: distribution of signal-to-noise ratio (S/N) as a function of the 20% level line width W_{20}. *Bottom*: rms noise σ in mJy (outside the 21-cm line) versus integration time. The curve shows the line $\sigma = 20/\sqrt{T_{\rm int}}$.

and $f_{\rm i}(\lambda)$ = 1.0, 0.59, 0.47, 0.30, 0.15 (Tully et al. 1998; Watanabe et al. 2001; Masters et al. 2003) for B, I, J, H, and K bands, respectively.

Radial velocities. All radial velocities were taken from Hyperleda, often a mix and an average of several publications

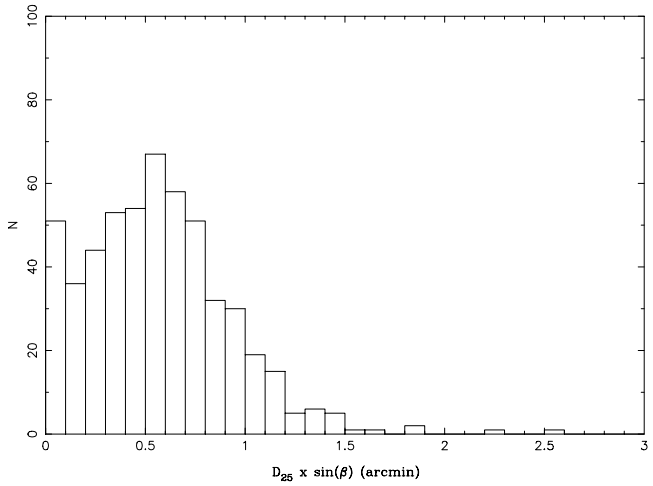

Fig. 3. Projection of the major axis D_{25} on the East-West direction.

and redshift surveys. Within the limit of 8000 km s^{-1}, we collected a sample of 32 545 galaxies. In general, when an HI measurement was available (i.e. for most of the TF subsample used in this study), the radio radial velocity was preferred, being more accurate than the available optical one. As normal in Hyperleda, when more than two redshift measurements for the same galaxy were available, the most discrepant ones were rejected from the mean. The radial velocities are used at the first iteration of the IND method as a reference distance scale for the Malmquist bias correction.

3.2. Selection and completeness

The analytical treatment of the Malmquist bias effect with distance, by applying the iterative normalised distance method, requires the strict completeness of the samples according to magnitude selection (Theureau et al. 1998b; and Sect. 4.). The limits in magnitude are simply determined by eye as the knee observed in a log N vs. magnitude diagram, witnessing the departure from a homogeneous distribution in space with growing distance. This limit is in "observed apparent magnitude", independent of extinction or opacity correction. These corrections are however taken into account further, as part of the normalised distance scheme itself, in what we call the effective magnitude limit (Sect. 4.1.).

The adopted completeness limits are the followings: $J_{\rm lim}$ = 12.0, $H_{\rm lim}$ = 11.5, and $K_{\rm lim}$ = 11.0 (equivalent to $B_{\rm lim} \sim 15$ and $I_{\rm lim} \sim 13$). Only the complete part of the sample in each band, about half of available data, is included for further study.

The final selection is made according to the following conditions:

- J, H, and K magnitudes <completeness limit;
- magnitude uncertainty <0.3 mag;
- log of rotational velocity uncertainty <0.03;
- T = 1–8 to keep only fair spiral galaxies;
- log $R_{25} > 0.07$ to avoid face-on galaxies for which the rotational velocity is poorly determined.

After these restrictions there are 3263 spiral galaxies distributed over the whole sky (see Fig. 5).

Fig. 4. 21-cm line profiles of galaxies listed in Table 2. Available only in electronic form at the CDS. Profiles are classified according to their PGC name written above each panel. Ordinate and abscissae axes are respectively graduated in km s^{-1} and Jy. Note that heliocentric radial velocities are expressed in terms of optical redshift $c\frac{\Delta\lambda}{\lambda}$. The horizontal line represents the baseline of the profile, i.e. the zero flux level, from which the maximum is estimated.

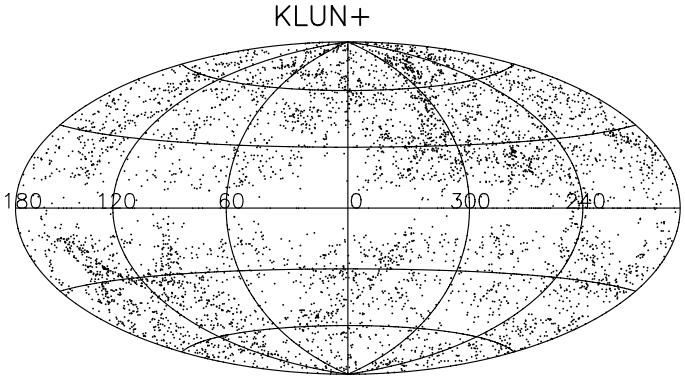

Fig. 5. Sky distribution of KLUN galaxies used in the current analysis.

4. Method of analysis

In this section we explain the Iterative Normalised Distance (IND) method for deriving the peculiar velocities. The "iterative" means that a previously calculated peculiar velocity field is used for more accurately estimating of new peculiar velocities. The "normalised distance" is a quantity depending on the distance and the absolute size or absolute magnitude of a galaxy, such that for any galaxy, the average selection bias (in the terminology of Strauss & Willick 1995) or the Malmquist bias of the second kind (according to Teerikorpi 1997) can be given by a function depending on its normalised distance, the dispersion of the distance criterion, and the completeness limit. This is illustrated in Fig. 6, where the TF residuals, plotted against the normalised distance modulus, clearly show the unbiased regime and the deviation due to the magnitude cutoff.

A detailed description of the method follows, but we start by listing the main steps:

1. calculate the absolute magnitudes and the normalised distances using the kinematical (redshift) distances;
2. calculate the TF relation using the unbiased part of the normalised distance diagram;
3. use the unbiased TF relations and the analytical Malmquist-correction formula for estimating real-space galaxy distances beyond the unbiased plateau limit (Fig. 5);
4. obtain the peculiar velocity field in a Cartesian grid in the redshift space by smoothing the individual peculiar velocities given by the Malmquist-corrected TF distances;
5. go back to step 1, and use the corrected kinematical distances by substracting the smoothed peculiar velocity field values from the redshift velocities.

This loop is repeated until converging values for the peculiar velocities are obtained. The peculiar velocities for all the galaxies do not converge nicely, though. We thus extract the most unreliable galaxies (about 4%) and recalculate the velocities with the reduced data set (see Sect. 4.4. and Fig. 6). As confirmed by the tests done with a mock sample in Sect. 4.6. outliers used to be mainly very low Galactitic latitude objects for which the corrected total magnitude is not well estimated from observed ones, and core cluster members whose observed radial velocity, used as kinematical distance at the first iteration, does not reflect their true distance at all, due to their strong motion in the cluster potential.

4.1. Kinematical distances, normalised distances, and absolute magnitudes

Let us define the kinematical distance modulus as

$$\mu_{\rm k} = 5 \log \frac{cz}{H_0} + 25, \tag{2}$$

where cz is the observed heliocentric redshift, corrected by the CMB dipole motion. The absolute magnitude is

$$M_{\rm k} = m_0^{\rm c} - \mu_{\rm k} \tag{3}$$

where $m_0^{\rm c}$ is the apparent magnitude, corrected for inclination, extinction, and cosmological effects, as stated in Eq. (10) of Paturel et al. (1997) (the cosmological correction is negligible for all galaxies in the present study).

If we consider that the TF relation is a linear law characterised by a given slope and a given dispersion (the zero-point being fixed either by some local calibrators or by adopting a value of H_0), and if we assume that the sample is actually complete up to a well-defined apparent magnitude limit, then the selection bias at a fixed $\log V_{\rm m}$ is only a function of the distance (see Teerikorpi 1984; Theureau et al. 1997, 1998b). In other words, the bias at a fixed $\log V_{\rm m}$ and at a given distance is only the consequence of the magnitude cut-off in the distribution of TF residuals and it moreover does not depend at all on the space-density law.

By normalising to a same luminosity class, i.e. a same $\log V_{\rm m}$ value, and by taking into account the variation of the actual magnitude cut-off with extinction, one can build a unique diagram showing the bias evolution with distance. The distances and magnitudes are then scaled so that a sharp edge is seen at the sample completeness limit.

The normalised distance modulus is defined as

$$X_{\rm n} = \mu_{\rm k} + (M_{\rm TF} - m_{\rm lim} + a_{\rm ext}) \tag{4}$$

where $M_{\rm TF}$ is the absolute magnitude of a galaxy, as given by the Tully-Fisher relation and $m_{\rm lim}$ is the apparent magnitude completeness limit. More explicitely, if we develop $M_{\rm TF}$ as $[a_1 \log V_{\rm m} + a_0]$, it appears that we indeed normalise to the same $\log V_{\rm m}$ and the same effective magnitude limit $m_{\rm lim}^{\rm eff} = m_{\rm lim} - a_{\rm ext}$. $X_{\rm n}$ can also be expressed as $M_{\rm TF} - M_{\rm lim}$, i.e. the difference between the TF absolute magnitude at a given $\log V_{\rm m}$ and the absolute magnitude cut off (in the TF residuals) at a given distance.

The normalised magnitude

$$Y_{\rm n} = M_{\rm TF} - M_{\rm k} = M_{\rm TF} - m_0^{\rm c} + \mu_{\rm k} \tag{5}$$

corresponds to the departure of the absolute magnitudes calculated on the basis of kinematical distances from the true mean value given by the TF relation. This residual contains the contribution of magnitude and $\log V_{\rm m}$ measurement errors, internal TF dispersion, and peculiar velocity.

Figure 6 shows normalised distance moduli vs. normalised magnitudes for the galaxies derived by the Tully-Fisher relation. The curve going through the points is the analytical bias solution $f(X_{\rm n}, \sigma_{\rm TF}, m_{\rm lim})$, while the vertical line shows the upper limit adopted for the unbiased normalised distance domain.

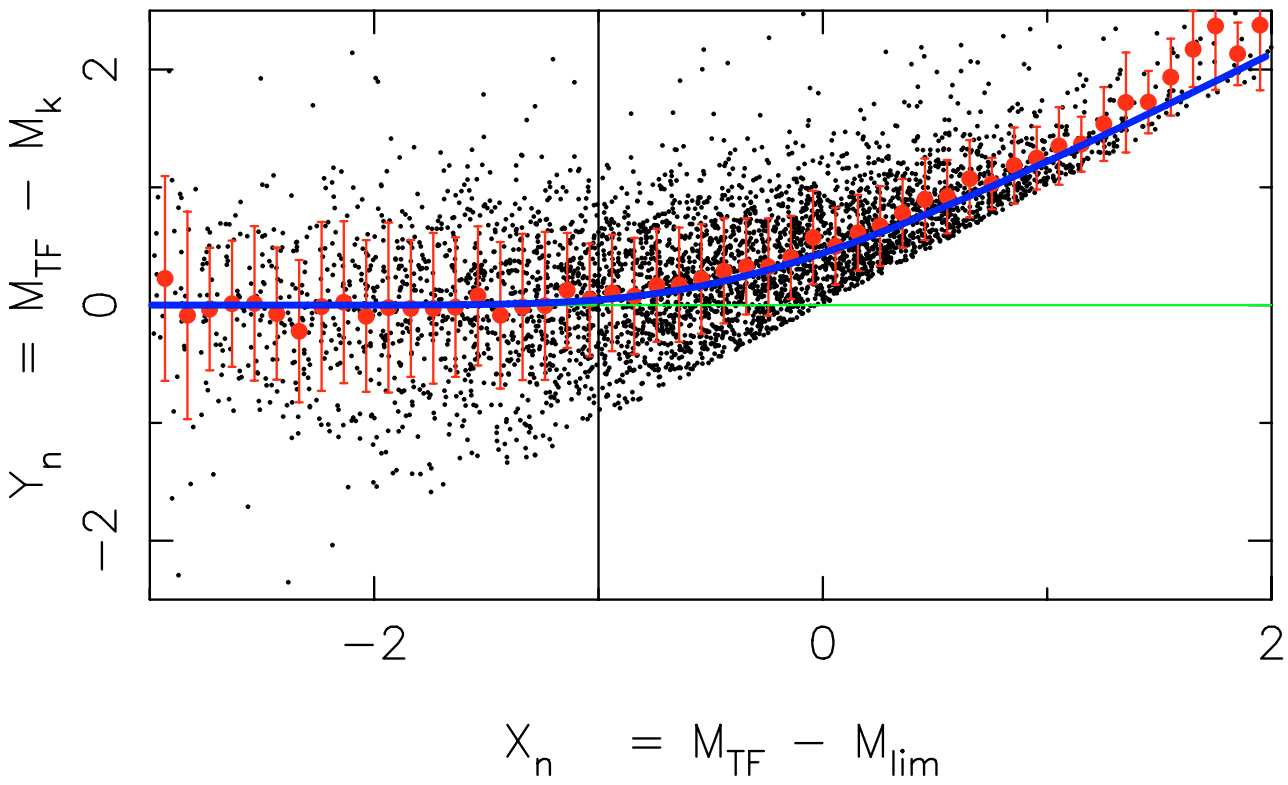

Fig. 6. TF residuals (Y_n against the normalised distance modulus (X_n). The "unbiased plateau" is the region at $X_n < -1$, where the binned average of the residuals, the balls with error bars, are close to the zero line. The curve going through the balls is the analytical correction formula described by Eq. (8) in Sect. 4.1.

4.2. Unbiased Tully-Fisher

The TF relation states the linear connection between absolute magnitude and $\log V_m$

$$M = a_1 \log V_m + a_0. \tag{6}$$

One gets the slopes, a_1, and zero-points, a_0, of the TF relations in each band (*IJHK*) by a least-square fit using the unbiased part of each sample. The unbiased part is the flat or plateau region in the normalised distance diagram. This subsample also provides us with the "0-value" of the TF residuals that are used to compute the bias deviation for the whole magnitude complete sample (Fig. 6). The method of deriving the TF relation in the unbiased plateau has been succesfully used in previous KLUN studies; a full statistical description can be found in Theureau et al. (1998b) and was even numerically tested by Ekholm (1997).

In the iterative scheme one starts by assuming a priori values for the TF slope and zero-point (here, only the slope is important and a rough value can be inferred directly from the whole sample). These values are used to compute the normalised distance and extract a first unbiased subsample. The loop "TF-slope → normalised-distance → unbiased-subsample → TF-slope" can be repated a couple of times to be sure to start on the basis of unbiased values.

4.3. Corrected distances

The function $f(X_n, \sigma_{TF}, m_{lim})$ is deduced from the expectancy of Y_n knowing X_n assuming that the magnitude selection $S(m)$ is described by the Heavyside function $S(m) = \theta(m - m_{lim})$. We have then:

$$E(Y_n|X_n) = \frac{1}{B}\int_{Y_{lim}}^{-\infty} \frac{1}{\sqrt{2\pi}\sigma} Y \exp\left[-\frac{Y^2}{2\sigma^2}\right] dY \tag{7}$$

where

$$\sigma = \sigma_{TF}$$

$$\begin{aligned} Y_{lim} &= Y_n(m_{lim}) = M_{TF} - m_{lim}^{eff} + \mu_k \\ &= M_{TF} - (m_{lim} - a_{ext}) + \mu_k \\ &\equiv X_n \end{aligned}$$

$$B = \int_{Y_{lim}}^{-\infty} \frac{1}{\sqrt{2\pi}\sigma} \exp\left[-\frac{Y^2}{2\sigma^2}\right] dY.$$

From here we derive:

$$f(X_n, \sigma, m_{lim}) = \sigma \sqrt{\frac{2}{\pi}} \frac{e^{-A^2}}{\mathrm{erfc}(A)} \tag{8}$$

where,

$$A = -\frac{1}{\sqrt{2}\sigma} X_n$$

and

$$\mathrm{erfc}(x) = \frac{2}{\sqrt{\pi}} \int_x^{-\infty} e^{-y^2} dy.$$

The corrected and unbiased distance modulus is then finally

$$\mu_c = m^c - M_{TF} + f(X_n, \sigma, m_{lim}).$$

Note that H_0 is cancelled out in $Y_{\rm lim}$. It is indeed hidden in the TF zero-point and explicitly present in μ_k but with an opposite sign.

The reader will notice that our approach to the bias in this paper is radically different to what has been attempted with MarkIII (Willick et al. 1997; or Dekel et al. 1999) in which the approach is from the viewpoint of the classical Malmquist bias (using in particular some inhomogeneous density correction).

4.4. Iterations

The peculiar velocities of galaxies are then smoothed onto a cartesian grid, $v_{\rm pec}(x, y, z)$ (Sect. 4.5). As explained above, the method relies on kinematical distances, and the normalised distances and the absolute magnitudes needed for TF relation include the kinematical distance. These distances can be made more accurate by subtracting the peculiar velocities from the redshift:

$$\mu_{\rm k} = 5 \log \frac{cz - v_{\rm pec}(x, y, z)}{H_0} + 25. \quad (9)$$

This distance modulus then replaces the value given by Eq. (2), and we can repeat the whole procedure with these updated distances. The new peculiar velocity field is again used for correcting the kinematical distances in the next iteration, and we keep on repeating the process until convergence.

In practice, subtracting the whole $v_{\rm pec}(x, y, z)$ as in Eq. (9) would overcorrect for the peculiar velocities and cause diverging oscillatory behaviour in the iterative process. Using a scaling factor $\lambda \in (0.0, 1.0)$, so that

$$\mu_{\rm k}^{j+1} = 5 \log \frac{cz - \lambda\, v_{\rm pec}^{j}(x, y, z)}{H_0} + 25, \quad (10)$$

removes this problem. The superscript j corresponds to the iteration number. Using the value $\lambda = 0.5$ we reach converging values after about 5–10 iterations. Figure 7 shows this convergence for a few galaxies. Usually the $v_{\rm pec}^{j}$ approaches a constant value nicely, in some cases the values oscillate even with high j. We checked all these convergence curves by eye and rejected the worst cases. With the restricted sample we recalculated the peculiar velocities and used the results of the selected 3126 spirals galaxies for the peculiar velocity mapping.

4.5. The tensor smoothing

After deriving radial peculiar velocities of galaxies, it is useful to interpolate these velocities at uniformly distributed grid points. The best method is to smooth the observed galaxy velocities with an appropriate window function. Dekel et al. (1999) discuss the problems of smoothing a non-uniformly distributed set of radial velocities:

The radial velocity vectors are not all pointing in the same direction over the smoothing window. Then, for example, in a case of a pure spherical infall towards the window centre, all the transverse velocities are observed as negative radial velocities. The net velocity in the smoothing window is then, incorrectly, negative, instead of being zero. Dekel et al. (1999) call this the tensor window bias. They find that it can be reduced by introducing a local velocity field with extra parameters, which is to be fitted for the observed radial velocities in the smoothing window. The best results are obtained by constructing a three-dimensional velocity field with a shear,

$$\boldsymbol{v}(\boldsymbol{x}) = \boldsymbol{B} + \boldsymbol{L} \cdot (\boldsymbol{x} - \boldsymbol{x}_{\rm c}), \quad (11)$$

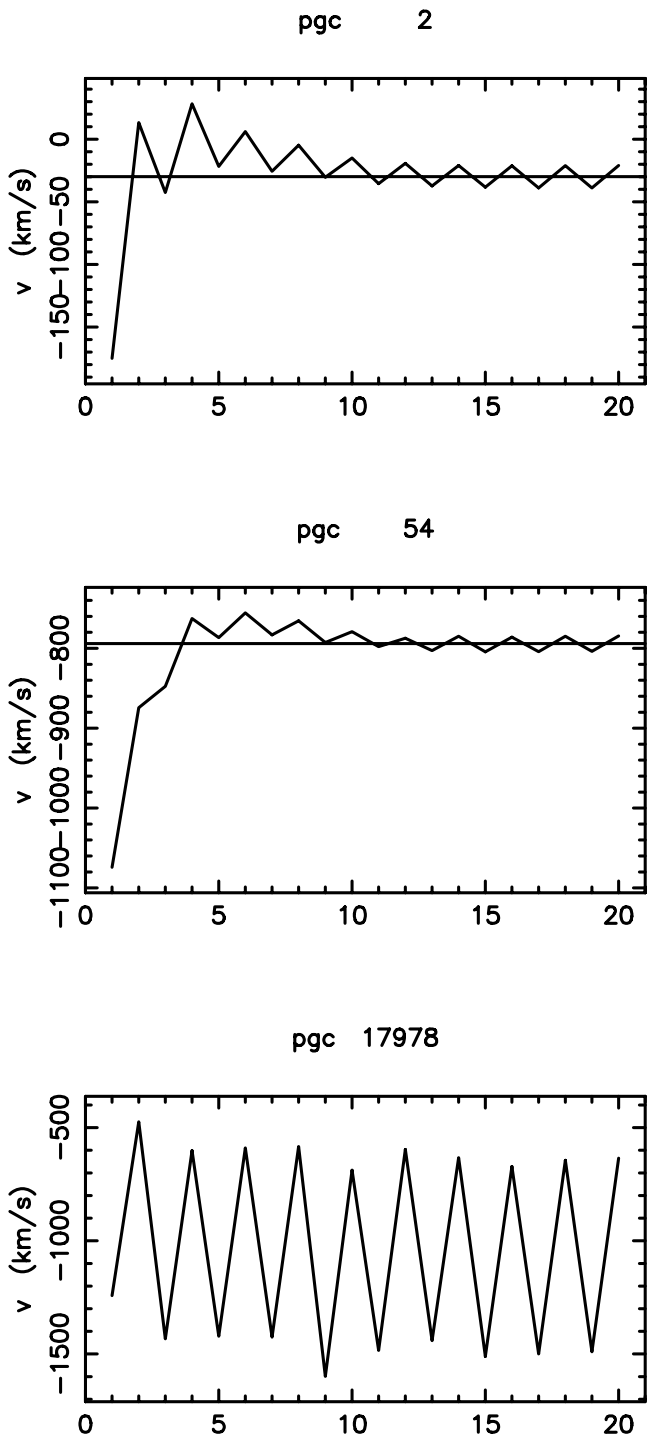

Fig. 7. The evolution of peculiar velocities with respect to the number of iterative loop. Here are the two first galaxies in our sample and an exceptionally "bad" case (pgc 17978) that was rejected from the final analysis.

where $\boldsymbol{L}$ is a symmetric tensor, and $\boldsymbol{x}_{\rm c}$ is the window-centre. There are then nine free parameters, three for the actual window center velocity $\boldsymbol{B}$ and the six components of the tensor $\boldsymbol{L}$. The resulting grid point velocity is just $\boldsymbol{v}(\boldsymbol{x}_{\rm c}) = \boldsymbol{B}$.

Furthermore, if the true velocity field has gradients within the effective smoothing window, a nonuniform sampling will cause an error called the sampling-gradient bias. Dekel et al. (1999) suggest that this bias can be diminished by weighting the observed galaxy velocities by the volume $V_{\rm n}$, which is defined

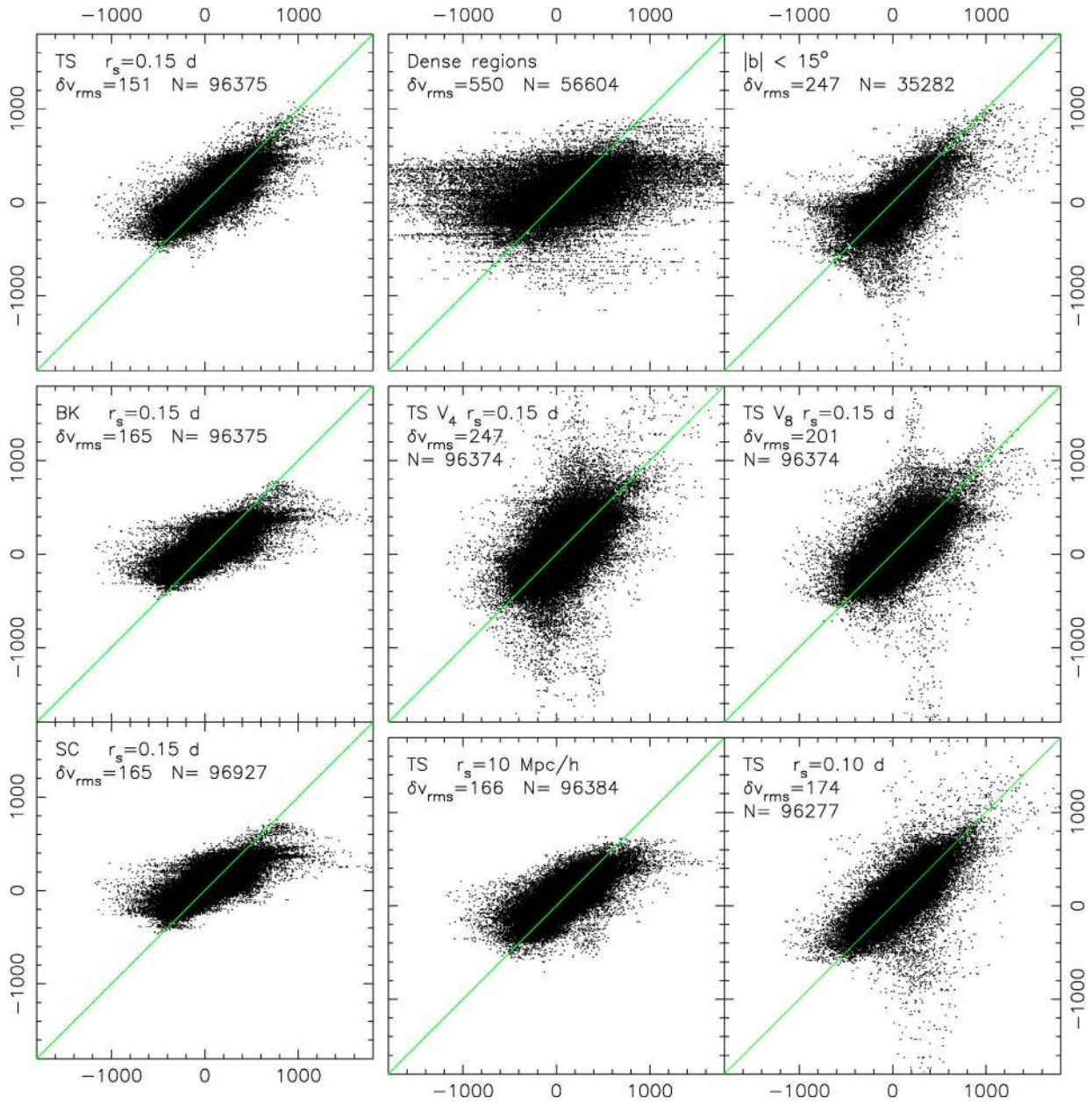

Fig. 8. The true peculiar velocities (on y axis) vs. the velocities obtained with a smoothing method for the GIF consortium simulated data. The upper left corner of each panel gives the essential information about the plot; TS stands for the tensorial smoothing, using nine parameters, the bulk velocity $\boldsymbol{B}$, and the tensor $\boldsymbol{L}$; BK is the three parameter bulk smoothing (only $\boldsymbol{B}$), and SC means scalar smoothing, using a simple Gaussian smoothing window. r_s is the smoothing radius, either a distance-dependent value, e.g. $0.15d$ or a fixed value, e.g. 10 Mpc h^{-1}. The rms difference between the smoothed and the true velocity field, $\delta v_{\rm rms}$, is given in km s^{-1}. N is the number of points, the simulated galaxies, in each figure. The upper left figure shows the smoothing giving the smallest $\delta v_{\rm rms}$. In each figure the galaxies in densest regions were excluded, as well as the objects at the low Galactic latitudes. The two panels in the upper right corner show how these points give substantially more divergent values. The "Dense regions" and "$|b| < 15°$" maps were obtained with the TS $r_s = 0.15d$ smoothing. V_4 and V_8 correspond to the volume weighted method, using the volume defined by the fourth and the eight closest galaxies, respectively. The volume weighting is claimed to reduce the sampling gradient bias, but in this test they fail to produce a better estimate of the true velocity field than the non-weighted method.

as the cube of the distance between the galaxy and its nth neighbour. This method gives more weight to galaxies in isolated areas.

4.6. Testing the method

We test these biases with a mock peculiar velocity catalogue. The mock catalogue is constructed from the GIF consortium constrained n-body simulation of our 80 h^{-1} Mpc neighbourhood (Mathis et al. 2002, `http://www.mpa-garching.mpg.de/NumCos/CR/`). The simulation was run for a flat ΛCDM cosmological model, and it provides locations, velocities, masses, and luminosities 189 122 galaxies, both with and without the internal absorption. The galaxy formation was defined by applying a semianalytic algorithm to the dark matter merger tree. We added the Galactic component of the absorption, as defined in Schlegel et al. (1998), and selected the galaxies brighter than a magnitude limit. In the end there are 9800 galaxies with their apparent B band magnitude smaller than 14.5.

Table 4. Tully-Fisher parameters: slope, zeropoint, scatter, and the number of unbiased plateau galaxies used in the relation.

	a_1	a_0	$\sigma_{\rm TF}$	N
J	–6.3 ± 0.31	–8.8 ± 0.14	0.46	960
H	–6.4 ± 0.33	–9.1 ± 0.14	0.47	1166
K	–6.6 ± 0.37	–9.0 ± 0.16	0.45	990

Figure 8 shows the true vs. smoothed peculiar velocities using different smoothing methods and a set of window parameters. These plots lead to the following comments:

- the scatter is mainly related to the smoothing radius;
- outliers are essentially;
  - galaxies at low Galactic latitude, for which the magnitude is not well-defined and where the sparser sampling leads the smoothing to diverge (vertical spreading);
  - galaxies belonging to clusters for which the kinematical distance derived from the redshift is strongly affected by the cluster velocity dispersion;
- one observes a tilt with respect to the line with slope = 1, when no tensor window is used. This is the effect of the velocity gradient around structures, and it leads to an underestimation of infall patterns and to a cooler velocity field.

The best χ^2 value is obtained for B + L smoothing, and $R_{\rm smooth}$ = 0.15 × distance. This will be our choice of smoothing for the rest of the study.

5. Preliminary results

In this section we present the TF relation parameters obtained for three wavelengths (*JHK*) and some examples of maps of radial peculiar velocity fields, superimposed on the distribution of galaxies. A more detailed kinematical study is beyond the scope of the present analysis and will be presented in a forthcoming paper.

5.1. TF parameters

Figure 9 shows the final TF relations for the galaxies in the unbiased part of the normalised distance diagram. Table 4 lists the parameters a_1 and a_0 and the scatter of the relation:

$$M = a_1 \log V_{\rm m} + a_0. \quad (12)$$

The observed scatter is comparable to what was found by Karachentsev et al. (2002) using 2MASS magnitudes. The small difference (we get slightly smaller σ's) can be explained easily by our optimisation of the kinematical distance scale through the iterative process described above. Accounting for the observed broadening due to apparent magnitude and $\log V_{\rm max}$ uncertainties and to the residual peculiar velocity dispersion affecting the kinematical distances, one obtains an internal scatter of ∼0.44 mag for the TF relation in B and ∼0.4 mag in K. This is 0.1 mag greater than in studies restricted to pure rotation curve measurements of $\log V_{\rm max}$. Here instead, a large majority of $\log V_{\rm max}$ measurement are from the width of global HI profiles. As we know, even once corrected for non-circular motions, this width is still determined by the shape of a galaxy's rotation curve, the distribution of HI gas in the disc, and the possible presence of a warp (Verheijen 2001), leading to a greater intrinsic Tully-Fisher scatter.

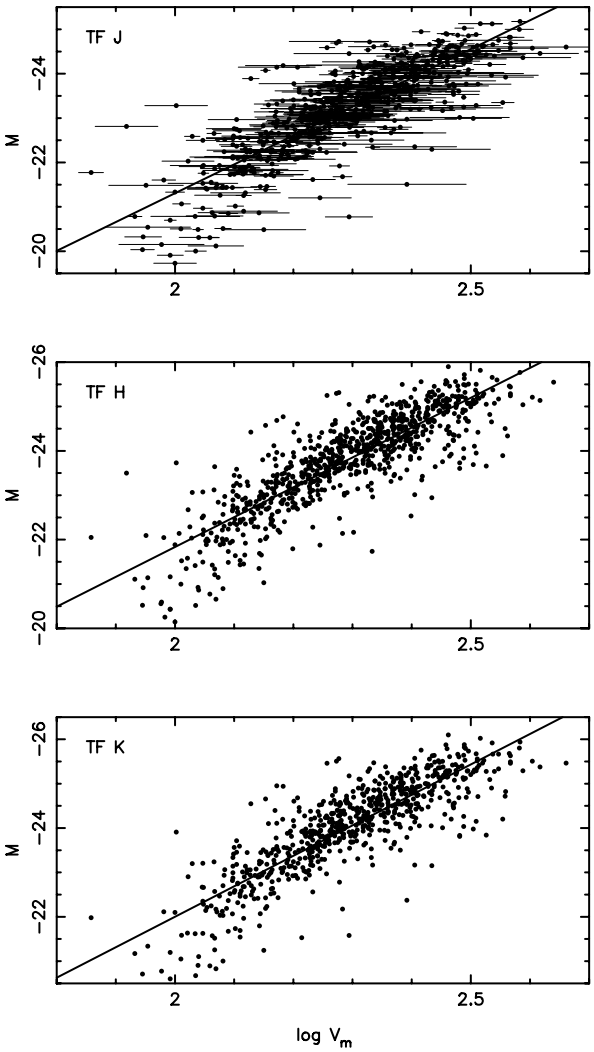

Fig. 9. Tully-Fisher relations in J, H, and K bands for unbiased plateau galaxies. See Table 4 for the parameters of the relations.

5.2. Peculiar velocities

Table 5 shows the KLUN+ galaxies with TF distances, together with their corrected kinematical distance, $d_{\rm k}^{\rm c} = V_{\rm 3k} - V_{\rm pec}$, which is our estimate of their true distance, and their observed redshift velocity, corrected to the CMB rest frame.

Our peculiar velocities were obtained for all points in space having a large enough galaxy density. We required that there be more than 15 galaxies with peculiar velocity measurements within the smoothing radius around the point. Then we fit the 9-parameter tensor field to the peculiar velocities of these galaxies and set the value obtained at the centre of the smoothing window (see Sect. 4 for more details).

Since we used a distance dependent smoothing radius, the points close the Local Group must have a higher density of KLUN galaxies around them than the more distant points, for a succesful velocity field determination. This explains why some of the more distant grid points have a set value, while there are apparently no galaxies around them.

We compared the data to the MarkIII distances (Willick et al. 1997). The Mark III catalogue was compiled from six samples of TF and one of elliptical galaxies. It was converted to a common system by adjusting the zero points of the distance indicators. For the Malmquist bias correction, the authors

Table 5. KLUN+ galaxies with TF distance. Columns 1 to 8 show the name and galactic coordinates, the three TF distance data from J, H, and K bands, the final estimate of the true distance, and the redshift velocity in the CMB frame. The distances are expressed in km s^{-1}. The full catalogue is available only in electronic form at the CDS.

Table 6. Directions, in Galactic coordinates, of some of the main bulk flow measurements or large galaxy concentrations, with numbers corresponding to Fig. 13 given in parentheses.

	l	b	Ref.
SNIa (1)	282	–8	Riess et al. (1997)
ENEAR (2)	304	25	da Costa et al. (2000a)
SFI+SCI+II (3)	295	25	Dale & Giovanelli (2000)
SMAC (4)	260	–1	Hudson et al. (1999)
PSCz (5)	260	30	Rowan-Robinson et al. (2000)
LP	343	52	Lauer & Postman (1994)
CMB	276	30	Local Group motion, Kogut et al. (1993)
GA	307	9	Great Attractor, Lynden-Bell et al. (1988)
HR	270	–55	Horologium–Reticulum, Lucey et al. (1983)
SC	315	29	Shapley Concentration, Scaramella et al. (1989)

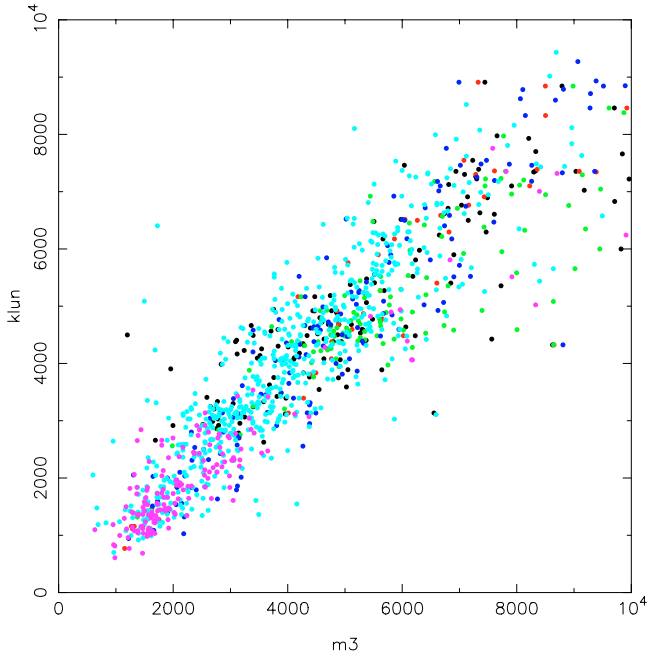

Fig. 10. Comparison of MarkIII and KLUN distances expressed in km s^{-1}. The colours represent the different Mark III samples (Willick et al. 1997): HMCL is black, W91CL red, W91PP green, CF blue, MAT turquoise, and A82 purple.

reconstructed the galaxy density field from the IRAS 1.2 Jy survey and used it for the inhomogeneous correction formula. The corrected distances for 2898 spirals and 544 ellipticals are publicly available and make a good comparison point for other peculiar velocity studies.

Figure 10 show the Malmquist corrected distances of individual galaxies, as measured in Mark III, versus the corresponding value derived by us. The relative scatter σ_d/d is ∼0.2, corresponding to an absolute uncertainty 0.43 in magnitude scale, is fully compatible with the measured TF scatter (see Table 4).

A few points in Fig. 10 show a clear mismatch. We found that these large discrepancies are due to errors in the input data in Mark III. These errors are listed and discussed in Appendix A.

Figure 11 shows the radial peculiar velocity field in the supergalactic plane, averaged over a disc with a thickness that increases towards the edge. The thickness of the disc in the centre is zero, and its opening angle is 15°, so that at the edge (at 80 h^{-1} Mpc) the disc width is about 20 h^{-1} Mpc. It is worth noting that in our $v_{\rm pec}$ maps one observes both the front and backside infall patterns around the main superclusters and structures. It is particularly obvious in Fig. 11 for the regions of Virgo, Perseus-Pisces, N533, Norma, or even Coma, although it is located close to the limit of the sample. It seems that we even detect an outflow on the front side of the Great Wall. Similar features are seen in Fig. 12 which shows other slices with different orientations in space.

A wide region, however, roughly centred on the Centaurus cluster, seems to move away from us at a coherent speed of ∼400 km s^{-1} on a scale greater than 20 h^{-1} Mpc. The direction and amplitude of this bulk motion are close to the one of the putative Great Attractor (Lynden-Bell et al. 1988; Hudson et al. 2004; Radburn-Smith 2006) and cannot be associated to any structure in particular. It does seem that this flow vanishes beyond a distance of 50 h^{-1} Mpc.

As an example of a quantitative result, we checked the amplitude and direction of a bulk flow within a growing sphere centered on the Local Group. The result is shown in Fig. 13. At short scales the direction of the flow is compatible with most previous studies (Table 6, Fig. 13, bottom panel). In particular, it coincides with the Great Attractor for $R \sim 20\ h^{-1}$ Mpc. On larger scales it first drifts towards the direction of the rich cluster region of Horologium-Reticulum, and after $R \sim 40\ h^{-1}$ Mpc back to $(l, b) \sim (310°, -8°)$.

In the upper panel, we show the bulk flow amplitude within a sphere of growing radius. It oscillates strongly on short scales, as a consequence of the density heterogeneity, and decreases to ∼250 km s^{-1} at 40 h^{-1} Mpc. Beyond this point it behaves more smoothly, as an indication that we have reached the scale of the largest structures within our sample. It starts to rise (or oscillate) again beyond 60 h^{-1} Mpc, probably due to the sparser space sampling.

The rms expected bulk velocity inferred from the standard ΛCDM model:

$$V_b^{\rm rms} = \langle v^2(R)\rangle^{1/2} = \left(\frac{\Omega_{\rm m}^{1.2}}{2\pi^2}\int_0^\infty P(k)\tilde{W}^2(kR){\rm d}k\right)^{1/2},$$

where $P(k)$ is the mass fluctuation power spectrum and $\tilde{W}^2(kR)$ the Fourier transform of a top hat window of radius R. For the parametric form of $P(k)$ in the linear regime, we used the general

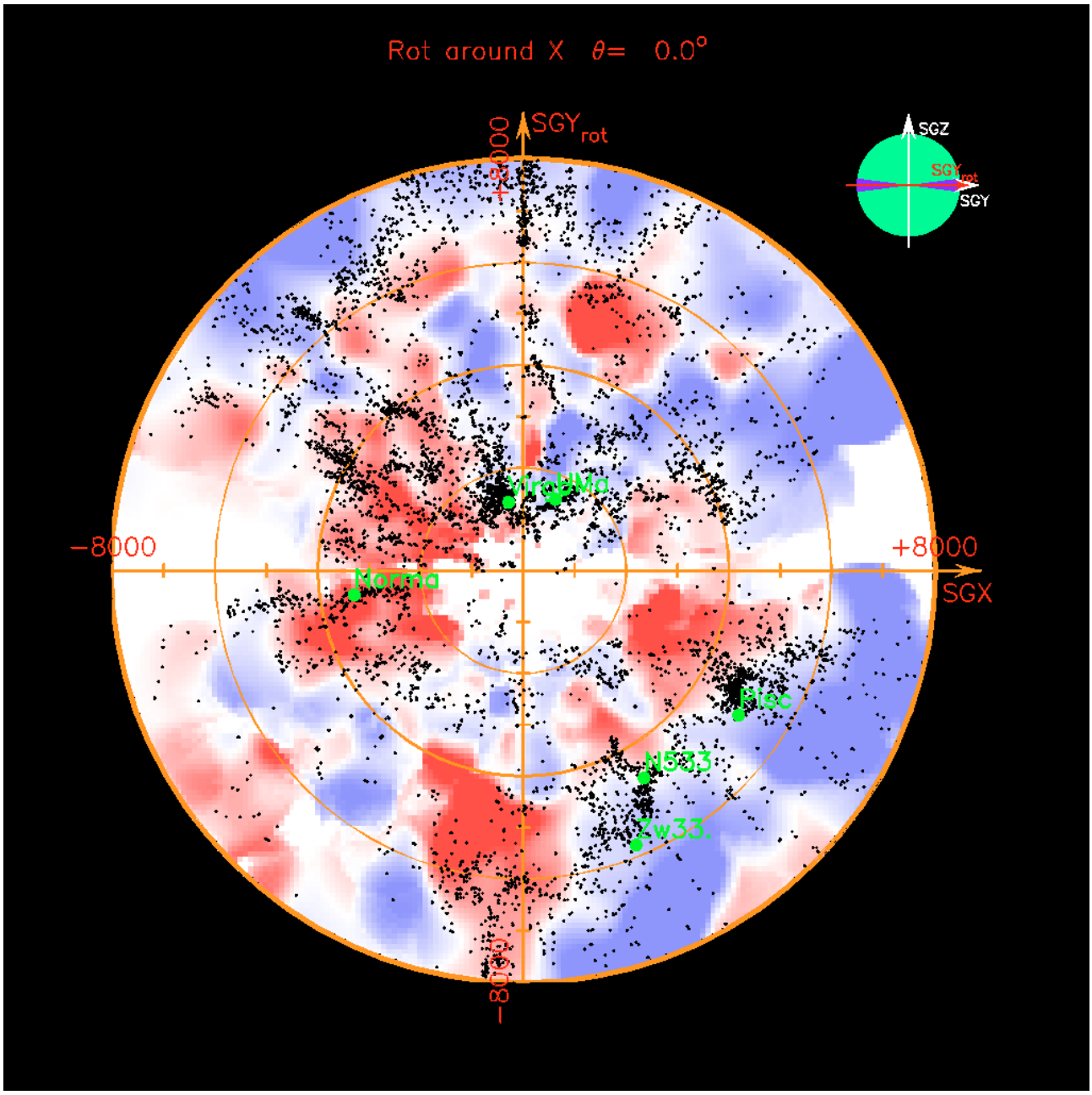

Fig. 11. Radial peculiar velocity field in the supergalactic plane. Blue colors are regions with negative peculiar velocities (infalling), red colors refer to positive ones (outfalling). The shade of the colour corresponds to the amplitude of the motion, and is saturated at 1000 km s^{-1}. The regions where the threshold requirement of at least two velocity measurements is not satisfied are set white. Black dots are all galaxies with a known redshift in Hyperleda. Green marks show positions of some well known structures – here Virgo, Ursa Major, Norma, Pisces, N533, and Zwicky33. The coordinates are in "real space", i.e. redshift distances corrected for the smoothed peculiar velocity field, in units of km s^{-1}.

CDM model (see e.g. Silberman et al. 2001):

$P(k) = A_c(\Omega_m, \Omega_\Lambda, n)T^2(\Omega_m, \Omega_b, h; k)k^n$

A_c is the normalisation factor and the transfer function $T(k)$ is the one proposed by Sugiyama (1995). We restricted the analysis to a flat cosmological model with $\Omega_m + \Omega_\Lambda = 1$, a scale-invariant power spectrum ($n = 1$), a baryonic density $\Omega_b = 0.04$ (WMAP result, e.g. Spergel 2006), a Hubble constant fixed at $h = 0.57$ (which is our own preferred value, inferred directly from primary calibration by Theureau et al. 1997)[6], adjusting only the value of Ω_m.

[6] Note that by construction the peculiar velocities themselves are independent of the choice of H_0.

The best fit has been obtained for $\Omega_m = 0.22$ in the distance range 40–60 Mpc, where the value of $\langle V_{rms}(R)\rangle$ appears very smoothed. We also plotted the ±0.02 curves around this best value. What we observe confirms the WMAP results for Ω_m (e.g. Spergel 2006) and seems coherent with the expected rms bulk velocity within a sphere for standard ΛCDM model (see e.g. Willick 2000; or Zaroubi 2002), thus with no bulk motion.

One should be prudent anyway in such kind of conclusion: the theoretical prediction is here the rms value of a quantity that exhibits a Maxwell distribution (see e.g. Strauss 1997); a single measurement of the flow field is only one realization out of this distribution and gives only very weak constraints on the cosmological model.

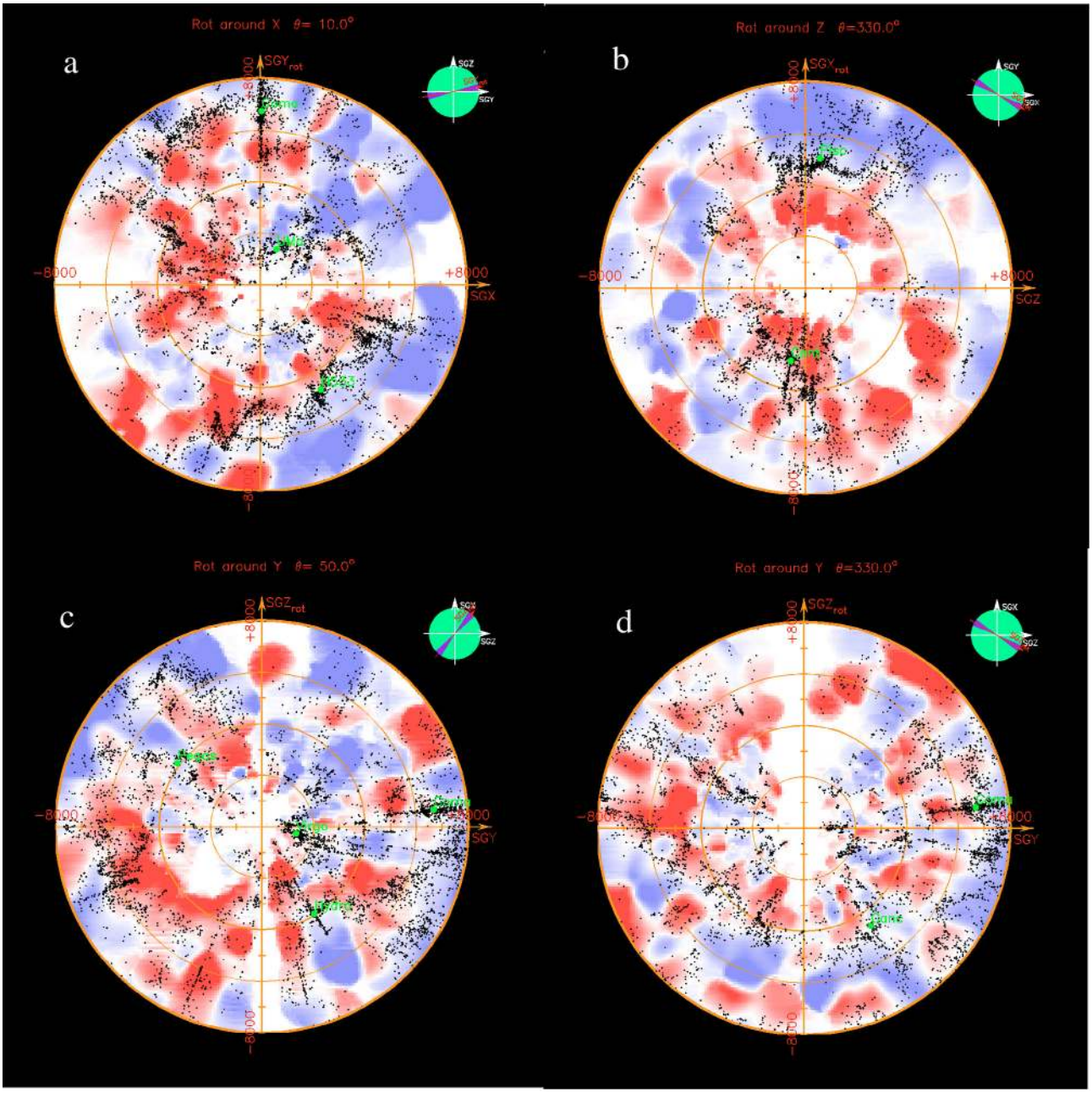

Fig. 12. The peculiar velocity maps, as in Fig. 11, projected on four discs of different orientations with respect to the supergalactic plane (SGZ = 0). **a)** Is rotated by 10° around the SGX axis. It illustrates the features well around two large rosary structures: the Great Wall starting from Coma and extending counterclockwise up to the Centaurus region, and another starting from the Perseus-Pisces complex, going down through N533 and beyond. Both front and backside infall are visible along the structures. **b)** Is rotated by −30° around SGZ from the SGY = 0 plane, and shows the large infall motions towards the two opposite regions, one in Perseus-Pisces and the other in the Great Attractor or Centaurus area. **c)** Rotated 50° around SGY from the SGX = 0 plane, shows the infall patterns towards Pegasus, Hydra, and Coma. **d)** Which is almost perpendicular to the supergalactic plane, rotated −30° around SGY from the SGX = 0 plane shows an example of some very detailed structures of the velocity field.

Acknowledgements. We have made use of data from the Lyon-Meudon Extragalactic Database (Hyperleda). We warmly thank the scientific and technical staff of the Nançay radiotelescope.

Appendix A: Mark III errata and rejections

When closely inspecting the Mark III data, we found a few inaccuracies. In comparison we used the Mark III catalogue provided by the CDS archives, `http://cdsweb.u-strasbg.fr`, cat. VII/198, and the data given by the Hyperleda database, `http://leda.univ-lyon1.fr`, as they were presented in May 2003. A few values in Mark III were replaced by those listed in Hyperleda. Some of the Mark III galaxies were rejected because of large differences to the Hyperleda values.

Table A.1 lists galaxies with their PGC numbers incorrectly identified in Mark III. We list first the number given in Mark III, followed by the correct number, alternative name, and the Mark III data set including the galaxy.

Table A.2 lists galaxies that were rejected due to their suspicious values for redshift velocities (values given in the CMB rest frame). All the galaxies with $|cz_{M3} - cz_{HL}| > 200$ km s^{-1} were studied, at most maintaining the Mark III values.

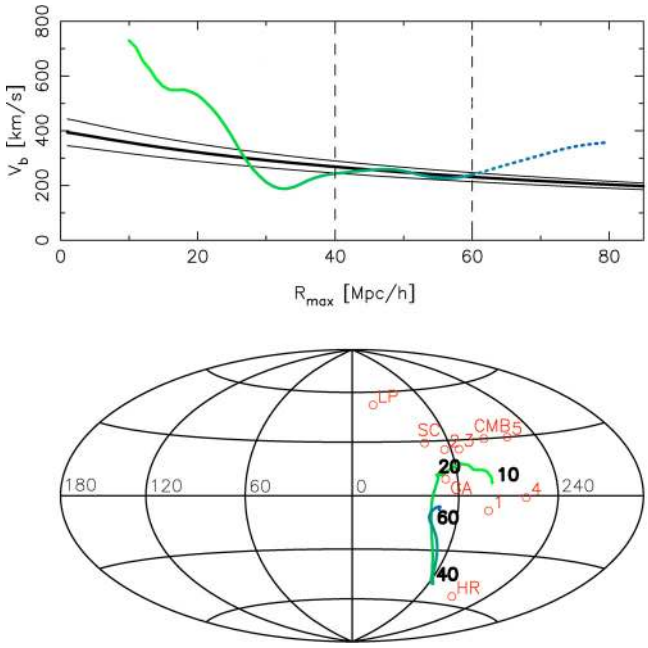

Fig. 13. *Upper panel* shows the amplitude of the observed bulk motion within a growing sphere of radius $R_{\rm max}$, and the corresponding ΛCDM expected curve for a flat cosmological model using: $n = 1$, $\Omega_{\rm b} = 0.04$, $h = 0.57$, and $\Omega_{\rm m} = 0.22 \pm 0.02$. The *bottom panel* shows the direction of the bulk flow in galactic coordinates and its evolution with $R_{\rm max} =$ 10–60 h^{-1} Mpc. The main published results as listed in Table 6 are also shown.

Table A.1. Mark III errata: PGC numbers.

Mark III	Correct	Alt. name	Mark III data sets
PGC 10631[1]	PGC 95735	–	HMCL, W91CL, CF
PGC 64575	PGC 64632	NGC 6902	HMCL
PGC 57053	PGC 57058	UGC 10186	W91CL
PGC 71291	PGC 71292	UGC 12572	W91CL

[1] PGC 10631 = UGC 2285 is projected on PGC 95735, but at lower redshift. Mark III clearly refers to the latter, but lists it as UGC 2285.

Table A.3 has the galaxies rejected due to the $\log V_{\rm m}$ uncertainties. Here we considered galaxies with $|\log V_{\rm m,M3} - \log V_{\rm m,HL}| > 0.15$. Notice that Mark III $\log W$ values are converted here to the inclination corrected $\log V_{\rm m}$ of Hyperleda.

Table A.2. Mark III errata: velocities.

	Mark III	Hyperleda	Mark III data sets
PGC 26680	7266	12736	HMCL
PGC 72301	11 747	7348	W91PP
PGC 17136[1]	4417	8870	CF
PGC 26561[2]	2136	1664	MAT
PGC 67258	2278	2684	MAT
PGC 62889	2513	5745	MAT
PGC 30753[3]	2946	3813	MAT
PGC 9551	4057	4633	MAT
PGC 20324[4]	4114	5681	MAT
PGC 15790	4202	6199	MAT
PGC 47832	4477	4827	MAT
PGC 31723[5]	4866	4130	MAT
PGC 62411[6]	5075	5996	MAT
PGC 5964	5859	5406	MAT
PGC 3144	5974	5053	MAT
PGC 8888	6070	5049	MAT
PGC 64523	6384	5271	MAT
PGC 19363	7092	6666	MAT
PGC 2001	7112	6180	MAT
PGC 44349	9696	9916	MAT

[1] Value incorrectly copied from the data source.
[2] Lower value suggested by three independent sources.
[3] See note at Giovanelli et al. 1997 (Antlia 27146).
[4] Possible confusion with galaxy 1′ SE.
[5] A typographical error in MAT file? See Mathewson et al. (1992; Fig. 3).
[6] Unclear Hα observation.

Table A.3. Mark III errata: $\log V_{\rm m}$.

	Mark III	Hyperleda	Mark III data sets
PGC 72024	2.321	2.131	HMCL,W91CL,W91PP,CF
PGC 47707[1,2]	2.139	2.391	HMCL
PGC 65338[1]	2.079	1.844	HMCL
PGC 7111[1]	1.978	2.251	HMCL
PGC 36875[1]	2.253	2.453	W91CL
PGC 9841[3]	2.049	1.596	W91PP
PGC 51784	2.209	1.889	CF
PGC 5453	2.429	1.980	CF
PGC 17113[1]	1.994	1.830	MAT
PGC 16201	1.807	2.092	MAT
PGC 32821[1]	2.023	1.861	MAT
PGC 67818[1]	2.052	1.843	MAT
PGC 39139	1.760	2.018	MAT
PGC 51982[1]	2.284	2.057	MAT
PGC 24328	2.232	2.013	MAT
PGC 64042[1]	2.442	2.200	MAT
PGC 13778[1]	2.295	2.123	MAT
PGC 2383	1.978	2.150	MAT
PGC 36875[1]	2.241	2.453	A82

[1] These galaxies have large differences in inclination stated in Mark III and in Hyperleda.
[2] Mark III states the inclination as 90°, while it is 34° in Hyperleda. The latter is probably correct.
[3] Several sources favour the Hyperleda value.

References

Barnes, D. G., Staveley-Smith, L., de Blok, W. J. G., et al. 2001, MNRAS, 322, 486
Bottinelli, L., Gouguenheim, L., Fouqué, P., & Paturel, G. 1990, A&AS, 82, 391
Bottinelli, L., Durand, N., Fouque, P., et al. 1992, A&AS, 93, 173
Bottinelli, L., Durand, N., Fouque, P., et al. 1993, A&AS, 102, 57 (Paper II)
da Costa, L. N., Bernardi, M., Alonso, M. V., et al. 2000a, ApJ, 537, L81
da Costa, L. N., Bernardi, M., Alonso, M. V., et al. 2000b, AJ, 120, 95
Dale, D. A., & Giovanelli, R. 2000, Cosmic Flows Workshop, ed. S. Courteau, & J. Willick, ASP Conf. Ser., 201, 25
Dekel, A., Eldar, A., Kolatt, T., et al. 1999, ApJ, 522, 1
Ekholm, T. 1996, A&A, 308, 7
Ekholm, T., Teerikorpi, P., Theureau, G., et al. 1999, A&A, 347, 99
Fouqué, P., Bottinelli, L., Gouguenheim, L., & Paturel, G. 1990, ApJ, 349, 1
Giovanelli, R., Haynes, M. P., Herter, T., et al. 1997, AJ, 113, 22
Guilliard, P. 2004, Master Thesis
Hanski, M. O., Theureau, G., Ekholm, T., & Teerikorpi, P. 2001, A&A, 378, 345
Haynes, M. P., Giovanelli, R., Chamaraux, P., et al. 1999, AJ, 117, 2039
Hudson, M. J., Smith, R. J., Lucey, J. R., Schlegel, D. J., & Davies, R. L. 1999, ApJ, 512, L79
Hudson, M. J., Smith, R. J., Lucey, J. R., & Branchini, E. 2004, MNRAS, 352, 61
Jarrett, T.-H., Chester, T., Cutri, R., et al. 2000, AJ, 120, 298
Karachentsev, I. D., Mitronova, S. N., Karachentseva, V. E., Kudrya, Yu. N., & Jarrett, T. H. 2002, A&A, 396, 431
Kogut, A., Lineweaver, C., Smoot, G. F., et al. 1993, ApJ, 419, 1
Lauer, T. R., & Postman, M. 1994, ApJ, 425, 418

Lucey, J. R., Dickens, R. J., Mitchell, R. J., & Dawe, J. A. 1983, MNRAS, 203, 545
Lynden-Bell, D., Faber, S. M., Burstein, D., et al. 1988, ApJ, 326, 19
Mamon, G., Giraud, F., Rassia, E., et al. 2004, in Maps of the Cosmos, International Astronomical Union. Symp., 216, held 14–17 July, 2003 in Sydney, Australia
Marinoni, C., Monaco, P., Giuricin, G., & Costantini, B. 1998, ApJ, 505, 484
Masters, K., Giovanelli, R., & Haynes, M. 2003, AJ, 126, 158
Mathewson, D. S., & Ford, V. L. 1996, AJ, 107, 97
Mathewson, D. S., Ford, V. L., & Buchhorn, M. 1992, ApJS, 81, 413
Mathis, H., & White, S. 2002, MNRAS, 337, 1193
Mitronova, S. N., Karachentsev, I. D., Karachentseva, et al. 2004, Bull. Spec. Astrophys. Observ., 57, 5
di Nella, H., Paturel, G., Walsh, A. J., et al. 1996, A&AS, 118, 311
Paturel, G., Andernach, H., Bottinelli, L., et al. 1997, A&AS, 124, 109
Paturel, G., Fang, Y., Petit, C., Garnier, R., & Rousseau, J. 2000, A&AS, 146, 19
Paturel, G., Petit, C., Prugniel, P., et al. 2003a, A&A, 412, 45
Paturel, G., Theureau, G., Bottinelli, L., et al. 2003b, A&A, 412, 57
Paturel, G., Vauglin, I., Petit, C., et al. 2005, A&A, 430, 751
Radburn-Smith, D. J., Lucey, J. R., Woudt, P. A., Kraan-Korteweg, R. C., & Watson, F. G. 2006, MNRAS, 369, 1131
Riess, A. G., Davis, M., Baker, J., & Kirshner, R. P. 1997, ApJ, 488, L1
Rowan-Robinson, M., Sharpe, J., Oliver, S. J., et al. 2000, MNRAS, 314, 375
Saunders, W., Sutherland, W. J., Maddox, S. J., et al. 2000, MNRAS, 317, 55
Scaramella, R., Baiesi-Pillastrini, G., Chincarini, G., Vettolani, G., & Zamorani, G. 1989, Nature, 338, 562
Schlegel, D. J., Finkbeiner, D. P., & Davis, M. 1998, ApJ, 500, 525
Silberman, L., Dekel, A., Eldar, A., & Zehavi, I. 2001, ApJ, 557, 102
Spergel, D. N., Beau, R., Dore, O., et al. 2006 [arXiv:astro-ph/0603449]
Springob, C., Haynes, M., Giovanelli, R., & Kent, B. 2005, ApJS, 160, 149
Strauss, M. A. 1997, in Critical Dialogues in Cosmology, Proceedings of a Conference held at Princeton, New Jersey, 24–27 June 1996 (Singapore: World Scientific), ed. N. Turok, 423
Strauss, M. A., & Willick, J. A. 1995, Phys. Rep., 261, 271
Sugiyama, N. 1995, ApJS, 100, 281
Teerikorpi, P. 1984, A&A, 141, 407
Teerikorpi, P. 1997, ARA&A, 35, 101
Theureau, G., Hanski, M., Ekholm, T., et al. 1997, A&A, 322, 730
Theureau, G., Bottinelli, L., Coudreau, N., et al. 1998a, A&AS, 130, 333
Theureau, G., Rauzy, S., Bottinelli, L., & Gouguenheim, L. 1998b, A&A, 340, 21
Theureau, G., Coudreau, C., Hallet, N., et al. 2005, A&A, 430, 373
Tully, R. P., Pierce, M. J., Huang, J., et al. 1998, AJ, 115, 2264
de Vaucouleurs, G., et al. 1991, Third Reference Catalogue of Bright Galaxies (Springer-Verlag)
Verheijen, M. A. 2001, ApJ, 563, 694
Watanabe, M., Yasuda, N., Itoh, N., Ichikawa, T., & Yanagisawa, K. 2001, ApJ, 555, 215
Willick, J. 2000, in Proceedings of the XXXVth Rencontres de Moriond: Energy Densities in the Universe (Éditions Frontières) [arXiv:astro-ph/0003232]
Willick, J. A., Courteau, S., Faber, S. M., et al. 1997, ApJS, 109, 333
Zaroubi, S. 2002, MNRAS, 331, 901